Effects of electrically conductive walls on turbulent magnetohydrodynamic flow in a continuous casting mold

Blishchik, Artem; Glavinić, Ivan; Wondrak, Thomas; van Odyck, Daniel; Kenjereš, Saša

DOI
10.1016/j.ijheatfluidflow.2022.108967

Publication date
2022

Document Version
Final published version

Published in
International Journal of Heat and Fluid Flow

International Journal of Heat and Fluid Flow 95 (2022) 108967

Contents lists available at ScienceDirect

International Journal of Heat and Fluid Flow

journal homepage: www.elsevier.com/locate/ijhff

Effects of electrically conductive walls on turbulent magnetohydrodynamic flow in a continuous casting mold

Artem Blishchik [a], Ivan Glavinić [b], Thomas Wondrak [b], Daniel van Odyck [c], Saša Kenjereš [a,*]

[a] Transport Phenomena Section, Department of Chemical Engineering, Faculty of Applied Sciences, Delft University of Technology and J.M. Burgerscentrum Research School for Fluid Mechanics, Van der Maasweg 9, 2629 HZ Delft, The Netherlands
[b] Department of Magnetohydrodynamics, Institute of Fluid Dynamics, Helmholtz-Zentrum Dresden-Rossendorf, Bautzner Landstraße 400, 01328 Dresden, Germany
[c] Tata Steel, PO Box 10000 1970 CA, IJmuiden, The Netherlands

ARTICLE INFO

Keywords:
MHD
Magnetic field
Lorentz force
OpenFOAM
Electrically conducting walls
Dynamic LES
Continuous casting

ABSTRACT

In the present study, we have performed a series of numerical simulations of the turbulent liquid metal flow in a laboratory-scale setup of the continuous casting. The liquid metal flow was subjected to an external non-uniform magnetic field reproducing a realistic electromagnetic brake (EMBr) effect. The focus of this research was on the effects of the finite electrical conductivity of Hartmann walls on the flow and turbulence in the mold. To be able to simulate distributions of the electric potential and current in both the fluid and solid wall domains, we applied our recently developed and validated in-house conjugate MHD solver based on the open-source code OpenFOAM. The dynamic Large Eddy Simulation (LES) method was used to simulate the turbulent flow. The results obtained for the neutral (non-MHD) and MHD cases over a range of the imposed EMBr strengths – all for the perfectly electrically insulated walls – were compared with the available Ultrasound Doppler Velocimetry (UDV) measurements. A good agreement between simulations and experiments was obtained for all simulated cases. Next, we completed a series of simulations including a wide range of the finite electric conductivities (ranging from a weakly to perfectly conducting wall conditions) of the Hartmann walls for a fixed value of the imposed EMBr. The obtained results demonstrated a significant influence of the electric wall conductivities on the flow and turbulence reorganization. It is expected that here provided insights can be applicable for the new generation of the laboratory- and real-scale continuous casting setups.

1. Introduction

Steel casting is one of the most important industrial processes that fills humanity's needs in this material widely used in a range of technological applications. Nowadays, the great majority of the produced steel is obtained with continuous casting (CC) technology. Although the continuous casting has been actively used since the 1950s, incessant efforts to improve the efficiency of the entire process and specific crucial parts are being made. One of these crucial parts is the transport of the highly turbulent liquid metal flow from a tundish to a casting mold through a submerged entry nozzle. It is recognized that various destructive phenomena occurring in the mold are responsible for a significant reduction of the product quality (Thomas and Zhang, 2001). These phenomena include excessively strong double-roll flow patterns or entrainment and entrapping of the slag particles from the mold free-surface. To make such a sensitive process more stable, several control tools, including in particular, the electromagnetic brake (EMBr), are used. The application of the electromagnetic brake, as an elegant non-invasive Magnetohydrodynamics (MHD) based control mechanism, is possible because of a high electrical conductivity of the liquid steel ($\sigma = \mathcal{O}(10^6)$ S/m), which will produce electric current within the fluid when subjected to an external magnetic field. Finally, interactions of the generated electric current and imposed magnetic field will produce a Lorentz force which will locally affect the velocity field, (Davidson, 2001; Thomas and Chaudhary, 2009; Kenjereš, 2018).

Experimental studies of the MHD phenomena of continuous casting are challenging due to the presence of extremely high temperatures of the liquid steel (approx. 1500°C). To circumvent these high temperatures, experiments utilizing alloys (such as galinstan, GaInSn) that are in a liquid state at room temperatures are designed, (Plevachuk et al., 2014). The remaining problem with this and similar alloys is their opaqueness, which prevents them from applications of the classic laser

* Corresponding author.
E-mail address: S.Kenjeres@tudelft.nl (S. Kenjereš).

https://doi.org/10.1016/j.ijheatfluidflow.2022.108967
Received 1 September 2021; Received in revised form 9 February 2022; Accepted 26 February 2022
Available online 5 April 2022

optics diagnostics tools such as Laser Doppler Anemometry (LDA) and Particle Imaging Velocimetry (PIV).

Despite numerous challenges, significant research progress was made during the last decade. Many numerical and experimental studies focusing on the EMBr mechanism have been reported in the literature. In the numerical studies of Chaudhary et al. (2012), Large Eddy Simulation (LES) method was used to analyze effects of the EMBr vertical position. It was demonstrated that by applying a magnetic field across the port stronger jets were created, while a double-ruler brake significantly suppressed turbulence intensity. Effects of the imposed magnetic field strength and depth of the submerged nozzle were numerically investigated in Li et al. (2015). When the magnetic field strengthened, the typical double-roll flow pattern was moved up, whereas the deeper SEN resulted in moving these rolls down. An interesting combination of the LES and a zero-dimensional model was applied in numerical studies of the origin of the self-sustained oscillations in a thin cavity mimicking the simplified continuous casting setup, (Righolt et al., 2015). The multi-phase simulations of effects of the argon bubbles injection on the removal of the inclusion at the meniscus (top surface) were investigated in Zhang et al. (2006) and Sarkar et al. (2018). It was shown that the injection of smaller bubbles resulted in larger inclusions. Furthermore, by increasing the flow rate of injected bubbles the meniscus velocity was also increased.

In Schurmann et al. (2019) authors reported on experiments with the Ultrasound Doppler Velocimetry (UDV) sensors, which they used to analyze the specific nozzle shape in generating a swirling flow. The same measuring technique was also used in Timmel et al. (2010) where the focus was on the imposed magnetic field effects on the resulting flow structure and turbulence. To be able to track the presence of the injected argon bubbles in the mold, a novel magnetic induction tomography (MIT) experimental technique was introduced in Wondrak et al. (2011). The improved multi-phase capabilities of the MIT sensors, able to provide both the phase and amplitude data, were recently reported in Muttakin and Soleimani (2020). Considering the control theory, the initial attempts of creating the control loop for the continuous casting process were mainly focused on maintaining the level of the liquid metal in the mold, (Graebe et al., 1995). In the more recent work of Abouelazayem et al. (2020), the concept of the industrial real-time controller, capable of adjusting flow structure, was proposed.

It should be noted that in a great majority of studies reported in the literature dealing with continuous casting assumed the presence of the fully electrically insulated walls. However, in the real-scale industrial continuous-casting mold, working conditions can significantly deviate from this assumption (e.g. due to a formation of the solidifying shells in the proximity of the walls). A very few numerical and experimental studies addressed effects of the electric wall conductivities, e.g. Miao et al. (2012) and Liu et al. (2018). In these studies, a single value of the characteristic ratio of the wall/fluid conductivities was considered, and it was concluded that a finite wall conductivity had a significant impact on the flow. The effects of different configurations of the wide and narrow conductive walls in a continuous-casting mold were numerically investigated in Vakhrushev et al. (2020). The authors considered also a single value of the finite wall conductivity ratio in addition to perfectly insulated and perfectly conductive walls. The turbulent flow in the mold was reported to be strongly suppressed in the case of the conductive walls. The impact of the various imposed magnetic field strengths on the meniscus flow in a continuous-casting mold was presented in Vakhrushev et al. (2021). Again, the walls with just a single value of the characteristic wall conductivity ratio were used. The strong effect of the meniscus flow acceleration and braking was demonstrated depending on the strength of the imposed magnetic field.

For generic MHD configurations (i.e. flows in rectangular channels or pipes), it was demonstrated that a change of the wall conductance can have significant impact on the flow and turbulence reorganization, as shown in Zhang et al. (2004), Smolentsev et al. (2010), Blishchik et al. (2021) and Blishchik et al. (2021). This lack of a wider range of studies dealing with the effects of the electrically conducting walls is associated with partial challenges in creating and executing proper working conditions. The experimental difficulties are associated with a necessity to have a complex multi-modular structure of the setup allowing a simple replacement of the walls. For the computer simulations, the particular challenges are in the necessity to integrate both fluid and solid wall domains (so-called conjugate MHD (Mistrangelo and Bühler, 2011)), which requires the development of advanced numerical algorithms. In the present work, to fill the existing gap in the literature regarding the possible effects of the finite wall conductivity ratios on the flow and turbulence reorganization, we will perform a series of numerical simulations of an existing laboratory-scale continuous casting setup. Currently, the wall conductivity ratio is not considered as a control mechanism in a real continuous casting process. However, we will demonstrate that accounting for various values of the wall conductivity ratio at the design stage of a CC setup can significantly change the flow pattern. First, we will perform simulations of the non-MHD case and MHD case with perfectly electrically insulated walls over a range of EMBr (i.e. different values of the imposed current to generate localized spatial distribution of the magnetic field) and will compare results with the available experimental data. Second, we will perform a detailed parametric study of various electric conductivities of the Hartmann walls for a fixed value of the EMBr strength, and will report on the flow and turbulence reorganization.

2. Governing equations and numerical details

2.1. Governing equations for a turbulent one-way coupled MHD flow

An incompressible single-phase electrically conductive fluid is considered. The fluid is subjected to the external constant non-uniform magnetic field resulting in the appearance of the contributing Lorentz force. The flow of an electrically conducting fluid can be described by conservation of the mass and momentum, as follows:

$$\nabla\cdot\mathbf{U} = 0 \tag{1}$$

$$\frac{\partial\mathbf{U}}{\partial t} + \left(\mathbf{U}\cdot\nabla\right)\mathbf{U} = -\frac{1}{\rho}\nabla p + \nu\nabla^2\mathbf{U} + \frac{1}{\rho}\mathbf{F_L} \tag{2}$$

where $\mathbf{U}$ is velocity, p is pressure, ν is the kinematic viscosity, ρ is density, and $\mathbf{F_L}$ is the Lorentz force. The liquid metal flow in continuous casting mold is expected to be highly turbulent $\left(Re = \mathcal{O}(10^4 - 10^5)\right)$, and special attention should be devoted to the correct turbulence prediction. In the present study, we adopt the dynamic Large Eddy Simulation (LES) approach. In the LES, spatially filtered governing equations Eqs. 1 and 2 can be written as:

$$\nabla\cdot\overline{\mathbf{U}} = 0 \tag{3}$$

$$\frac{\partial\overline{\mathbf{U}}}{\partial t} + (\overline{\mathbf{U}}\cdot\nabla)\overline{\mathbf{U}} = -\frac{1}{\rho}\nabla\overline{p}^{*} + \nu\nabla^2\overline{\mathbf{U}} - \nabla\cdot\overline{\bar{\tau}}_{sgs} + \frac{1}{\rho}\overline{\mathbf{F}}_{\mathbf{L}} \tag{4}$$

where $(\overline{\bar{\tau}}_{sgs})$ is the sub-grid scale (SGS) stress tensor, ('$-$') is the spatially filtered value, and $\overline{p}^{*} = \overline{p} + \frac{1}{3}\tau'\mathbf{I}$ is the modified pressure. In order to close Eq. (4), the linear dependency of the SGS stress tensor on the strain rate is introduced:

$$\tau_{ij}^{sgs} = -2\nu_{sgs}\overline{S_{ij}}, \quad \nu_{sgs} = (C_S\Delta)^2\left(2\overline{S}_{ij}\overline{S}_{ij}\right)^{\frac{1}{2}} \tag{5}$$

where C_s is the Smagorinsky coefficient, $\overline{S}_{ij}$ is the strain rate tensor, ν_{sgs} is the sub-grid scale turbulent viscosity. Assuming C_s to be a constant would be not correct, considering the strong influence of the magnetic field on the flow fluctuations, (Krasnov et al., 2008). Hence, the dynamic approach proposed by Lilly (1992), representing the local calculation of C_s, is applied as follows:

$$C_S^2 = \frac{1}{2}\frac{\langle\langle L_{ij}M_{ij}\rangle\rangle}{\langle\langle M_{ij}M_{ij}\rangle\rangle} \tag{6}$$

$$L_{ij} = \widetilde{\overline{U}_i\overline{U}_j} + \widetilde{\overline{U}}_i\widetilde{\overline{U}}_j \tag{7}$$

$$M_{ij} = \Delta^2\widetilde{\overline{S}\overline{S}_{ij}} + \widetilde{\Delta}^2\widetilde{\overline{S}}\widetilde{\overline{S}}_{ij} \tag{8}$$

where Δ is the main filter ($\Delta = (\Delta_x\Delta_y\Delta_z)^{1/3}$), $\widetilde{\Delta}$ is the second filter ($\widetilde{\Delta} = 2\Delta$) and '$\langle\langle\ldots\rangle\rangle$' indicates the local spatial averaging operation over the cell faces.

The accounting of the MHD interactions is accomplished through the Lorentz force term, formulated as:

$$\overline{\mathbf{F}}_\mathbf{L} = \overline{\mathbf{J}} \times \overline{\mathbf{B}} \tag{9}$$

where $\overline{\mathbf{J}}$ is the current density, and $\overline{\mathbf{B}}$ is the constant imposed magnetic field. To calculate the new additional unknown variable $\overline{\mathbf{J}}$, we refer to the liquid metal nature of the fluid implying the extremely high magnetic diffusion and subsequently the very low magnetic Reynolds number:

$$Re_m = \frac{UD}{\lambda} \ll 1 \tag{10}$$

where Re_m is the magnetic Reynolds number, D is the characteristic length and λ is the magnetic diffusion. Following the statement in Eq. 10, the one-way coupling MHD approach can be applied starting from the Ohm law for the moving conducting fluid as:

$$\overline{\mathbf{J}} = \sigma(-\nabla\overline{\phi} + \overline{\mathbf{U}} \times \overline{\mathbf{B}}) \tag{11}$$

where σ is the electrical conductivity of the fluid and $\overline{\phi}$ is the electric potential. By substituting the divergence-free condition for the current density into Eq. (11), the Poisson equation for the electric potential can be formulated as:

$$\nabla^2\overline{\phi} = \nabla\cdot(\overline{\mathbf{U}} \times \overline{\mathbf{B}}) \tag{12}$$

The pressure-driven MHD flows are defined with two characteristic non-dimensional numbers, Reynolds and Hartmann numbers that are calculated as:

$$Re = \frac{UD}{\nu}, \quad Ha = BD\sqrt{\frac{\sigma}{\rho\nu}} \tag{13}$$

To conserve $\overline{\mathbf{J}}$, the Four Steps Projection Method (FSPM), proposed by Ni et al. (2007), is implemented in our code. Further key details of the numerical implementation are given in our recent work (Blishchik et al., 2021).

2.2. Modeling of the finite electrically conductive walls

Taking into account the finite electric conductivity and finite thickness of surrounding walls is not a trivial task, and requires a specific approach aimed at predicting the electric potential and current density transfer between fluid and wall domains. In the present study, we use our recently developed conjugate MHD method. Here, a brief summary of this approach is provided, while the complementary steps of the algorithm, as well as the thorough validation, can be found in Blishchik et al. (2021). The conjugate MHD method is generally based on splitting fluid and wall regions into different computation domains, where the Poisson's equation for the electric potential in different domains is formulated as:

$$\nabla\cdot(\sigma_L\nabla\overline{\phi}_L) = \nabla\cdot(\sigma_L(\overline{\mathbf{U}} \times \overline{\mathbf{B}})) \tag{14}$$

$$\nabla\cdot(\sigma_S\nabla\overline{\phi}_S) = 0 \tag{15}$$

where subscripts L and S indicate the liquid and solid domain, respectively. The specific weighted flux interpolation scheme is used to obtain the electric potential at the interface, (Weber et al., 2018):

$$\overline{\phi}_{i[L,S]} = w\overline{\phi}_L + \Big(1-w\Big)\overline{\phi}_S, \quad w = \frac{r_S\sigma_L}{r_L\sigma_S + r_S\sigma_L} \tag{16}$$

where r is the corresponding first cell-center distance from the interface. For the conjugate MHD problems, it is convenient to introduce additional non-dimensional parameter (C_d)) representing the characteristic electric conductivities and thickness ratios as:

$$C_d = \frac{\sigma_S d_w}{\sigma_L D} \tag{17}$$

where d_w is the characteristic thickness of the wall and D is the characteristic length-scale of the fluid domain.

2.3. The computer code

To carry out the simulations, we used our in–house finite-volume MHD solver based on the open-source library OpenFOAM (Weller et al., 1998). The solver includes all described conjugate MHD equations, (Blishchik et al., 2021). The spatial discretization for the convective and diffusive term is performed by using the second-order central differencing scheme (CDS), while the second-order temporal discretization is accomplished by using the backward scheme. The PISO algorithm (Issa et al., 1986) is applied to couple pressure and velocity fields.

3. Mini-LIMMCAST setup and boundary conditions

3.1. Experimental setup

In the present study, the geometry used for the numerical simulations is based on the most recent version of the laboratory-scaled mold of a continuous caster at Mini-LIMMCAST (Liquid Metal Model for Continuous Casting) facility located at Helmholtz-Zentrum Dresden-Rossendorf (HZDR), (Schurmann et al., 2018). The experimental details are only briefly provided here, while the detailed information is available in Schurmann et al. (2018). The eutectic alloy galinstan (GaInSn) is used as a model of liquid steel since it is liquid at room temperature, and has similar physical and electrical properties to liquid steel. Liquid metal is continuously driven from the reservoir to the tundish, where it enters the mold through the submerged entry nozzle (SEN), and then moves back to the reservoir. The flow rate through the SEN is controlled by the stopper rod, while the liquid metal level in the mold is kept constant. Two coils, one adjacent to each wide face of the mold, generate the electromagnetic braking (EMBr) effect 0.075 m below the free surface, Fig. 1. The strength of the generated magnetic field depends on the

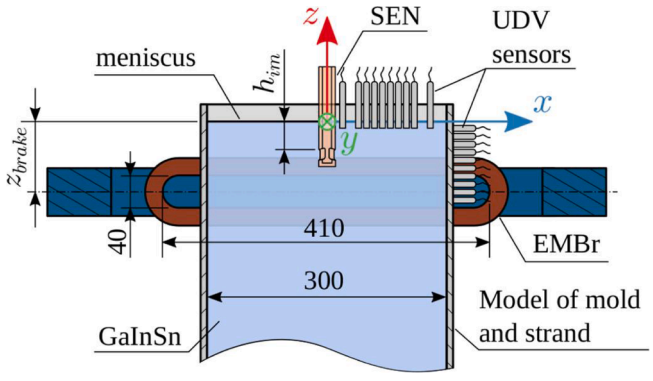

Fig. 1. Sketch of the experimental setup, (Schurmann et al., 2018). Note that the setup dimensions are defined. in millimeters.

electric current through the coils and can reach up to $B = 0.4$ T for the maximum current of $I = 600$ A. Walls in the experiment are considered as electrically insulated, i.e. $C_d = 0$. Velocity measurements are performed by using Ultrasound Doppler Velocimetry (UDV) with an array of ten ultrasound transducers on the upper part of the narrow wall. One should take into account that UDV can measure the velocity along the entire length of the beam but only the component in the axial direction of each transducer (the x-component for the present case) and the velocities are spatially averaged depending on the diameter of the ultrasound beam (which is 8 mm for the present setup).

3.2. Numerical setup

There is no need to consider a tundish and a reservoir in the numerical study, and consequently, the setup can be greatly simplified. The numerically simulated Mini-LIMMCAST domain will include the submerged entry nozzle with a bifurcated port and a rectangular mold, as shown in Fig. 2(a). The numerically simulated geometry is identical to the experimental setup: (i) the distance from the outlet to the meniscus $L = 0.612$ m, (ii) the width of the mold $W = 0.3$ m, (iii) the half-thickness of the mold $D = 0.0175$ m. It is important to note that these dimensions are valid only in the case of the electrically insulated solid walls. By inserting inside the mold two finite, electrically conducting, and perpendicular to the y-direction walls with the finite wall thickness $d_w = 5 \times 10^{-4}$ m, resulting half-thickness of the mold will be reduced to $D = 0.017$ m, Fig. 2(b). The SEN immersion depth $h_{im} = 0.35$ m remains constant. The numerically simulated port shapes are slightly less round than in original experiments resulting in a superior mesh quality (much less skewed control volume mesh in the proximity of the port). Note that this slight change of the port shape has not produced any notable changes in the flow and turbulence predictions.

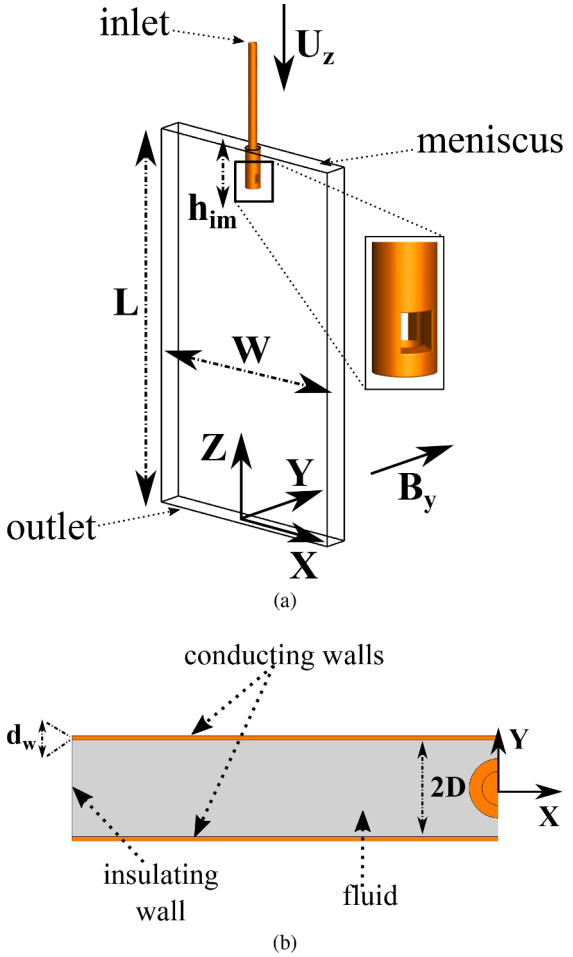

Fig. 2. Sketch of the numerical setup: (a) a side view of the entire mold, (b) a top view (from meniscus) of the mold (note that only half of domain is shown).

3.3. Mesh and boundary conditions

The constant flow rate obtained from the experiment $Q_{flow} = 7.17 \times 10^{-5}$ m^3/s is imposed at the inlet, and the zero-pressure boundary condition at the outlet. Although the bifurcated port is a natural turbulence generator, the turbulent structures need to be initialized before the port to mimic the real conditions where the flow is already turbulent in the SEN because of the flow disturbances generated by the stopper rod. In the present work, a fully developed turbulence state is obtained by imposing periodic boundary conditions at the upper part of the inlet segment. The no-slip velocity boundary condition is applied at all walls. The meniscus is modeled by imposing the slip-free boundary conditions. This approach proved to be the most numerically efficient and accurate because of a relatively small free-surface deformation observed in the experiments. Lastly, to generate electro-magnetic braking in the mold, the external magnetic field spatial distribution is imposed based on the measured B_y component of the external magnetic field in the z-coordinate direction, as indicated in Fig. 3. We divide our simulations into two groups. The first group includes the electrically insulating walls ($C_d = 0$, $\partial\phi/\partial n = 0$) and direct comparisons with the experiments over a range of imposed electric current ($0 \leqslant I \leqslant 375$ A) and resulting magnetic field strength ($0 \leqslant Ha \leqslant 210$). The second group of simulations includes activation of the conjugate MHD where the electric conductance of the Hartmann walls is varied over a wide range of the conductance wall parameter ($0.025 \leqslant C_d \leqslant 5$) with a fixed value of the imposed current of $I = 225$ A. Note that the wall conductivity ratio of the solidifying shell forming on the walls during the real size caster is $C_d \approx 0.125$. Additionally, the extreme case with $C_d \to \infty$ is considered as well (where $\phi = 0$ boundary condition is imposed), indicating the fully electrically conducting walls. The experimental data are not available for the second group of simulations but generated numerical results are intended to guide the design of a new generation of experimental setups with a finite conductance of the Hartmann walls. An overview of performed simulations is given in Table 1.

For the conjugate MHD cases (i.e. a finite C_d), the computational domain contains the fluid occupying and solid-wall (two Hartmann walls) regions. ICEM CFD meshing software is used to generate a block-

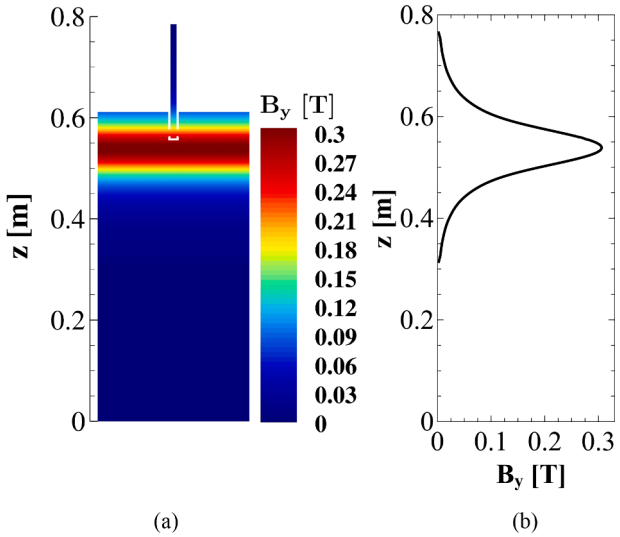

Fig. 3. (a) The contours of the B_y component of the magnetic field in the central vertical cross-section ($y = 0$ m); (b) the vertical profile of the B_y component of the magnetic field; Note that shown magnetic field is for imposed electric current of $I = 375$ A.

Table 1
List of simulations performed in the present study.

Group	Re	Ha	EMBr (in A)	C_d (Hartmann walls)
I	32000	0	0	0
		68	100	0
		142	225	0
		210	375	0
II	32000	142	225	0.025
		142	225	0.05
		142	225	0.1
		142	225	0.15
		142	225	0.2
		142	225	0.5
		142	225	1
		142	225	5
		142	225	∞

structured non-uniform mesh containing regular hexagonal control volumes (CVs). The fluid domain is represented by $M_L \approx 4 \times 10^6$ control volumes, while the solid-wall domain contains $M_S \approx 5 \times 10^5$ control volumes, Fig. 4.

The mesh refinement is applied in the proximity of the walls, meniscus at the top, as well as around the entrance ports of the nozzle. In the present study, we apply the Spalding wall functions for the wall treatment (Spalding, 1961). To check the grid dependency of obtained solutions two additional numerical meshes are also considered: the coarse mesh, with $M_{L,coarse} \approx 2 \times 10^6$ CVs, the fine mesh $M_{L,fine} \approx 6 \times 10^6$ CVs, Appendix A. The Courant number $Co = (\Delta t/2V)\sum_{faces}\left|\psi_i\right| \approx 1$ is kept for all simulations (note that V is the cell volume and ψ is the face volumetric flux).

4. Results and discussion

4.1. Validation with the experiment for the electrically insulated walls

We start our analysis by comparing numerical simulations and experimental results for cases with the electrically insulated walls (group I results as listed in Table 1). The most salient long-term averaged flow features are shown in Fig. 5, where we select the central vertical cross-section and superimpose the streamlines and contours of the velocity magnitude for various strengths of the imposed EMBr (i.e. $0 \leqslant I \leqslant$ 375 A). To obtain a reliable convergence of the first- and second-moments of the velocity field statistics, we perform averaging over 120 s after the initial flow establishment. It can be seen that flow has a typical double-roll structure in the upper and lower parts of the mold. By imposing the electric current of $I = 100$ A, Fig. 5(b), the centers of the lower rolls are more shifted in the negative z-direction compared to the neutral case, Fig. 5(a), while the upper rolls stay unaffected. With further increase of the applied current, the lower rolls are significantly reduced and their centers are moved closer to the inlet port, Figs. 5(c), (d). In contrast, locations of centers of upper rolls are just slightly affected by imposed changes of electric current.

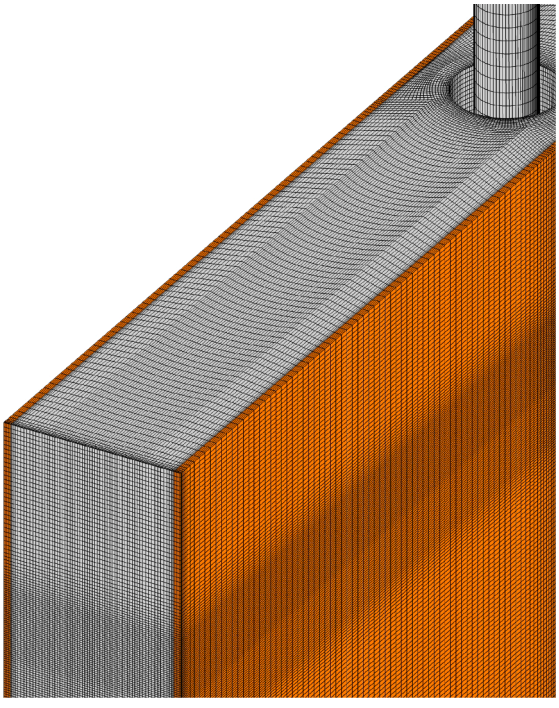

Fig. 4. The numerical mesh in the upper-left part of the mold. The fluid region is colored by grey, the solid region is colored by orange.

Next, we compare measured and numerically obtained vertical profiles of the mean streamwise (in the x-coordinate direction) velocity component in the central vertical plane ($y = 0$ m) at characteristic horizontal locations: $x = 0.04, 0.06, 0.08, 0.1$ m, as illustrated in Fig. 6. To make a direct comparison between measurements and numerical simulations, we also perform spatial averaging of simulations data in a form of the cylindrical shape (mimicking UDV beam) with typical radius of $r_{av} = 4 \times 10^{-3}$ m and the height $h_{av} = 0.5 \times 10^{-3}$ m.

The comparison between velocity profiles for various strengths of the imposed electric currents is shown in Fig. 7. The profiles exhibit typical behavior of a spreading jet with a characteristic peak diminishing with the distance from the nozzle. For the neutral case ($I = 0$ A), a good agreement is obtained at all locations, Fig. 7(a). With the magnetic field activation, the jet angle changes because of the Lorentz force effect (due to the electrically insulated walls, the current density loops are closing within the fluid domain, giving stronger Lorentz force and producing jet acceleration). This results in a characteristic jet peak increase in magnitude, with its location closer to the meniscus, and stronger penetration within the mold, Fig. 7(b-d). Similar behavior of the flow was previously also observed in experimental studies of Schurmann et al. (2018). An overall good agreement is obtained at practically all considered locations. Some differences in the proximity of the meniscus at x = 0.04, 0.06 and 0.08 m locations are visible for the strongest applied current of $I = 375$ A, Fig. 7(d). This can be explained by dampening of the experimentally measured velocity in the proximity of the meniscus caused by the formation of the oxide layer, which will affect the current distribution within the mold, and consequently, in the lower velocity there. Note that all results presented here are for the intermediate numerical mesh since it proved to be adequate, as shown in the grid dependency analysis in Appendix A.

4.2. The influence of the wall conductivity on the flow structure

To study the effects of the finite electric conductivity of the Hartmann walls on flow and turbulence, we perform series of numerical simulations from group II (Table 1), where we vary the wall conductance ratio with a fixed imposed electric current of $I = 225$ A. This intermediate current intensity is selected since it proved enough to impose some significant effects on the flow and turbulence for the electrically insulated walls. The long-term time-averaging is performed for 100 s, which proved to be sufficient to get reliable convergence of the flow statistics.

The mean velocity fields in the central vertical plane for different values of the wall conductance parameter are shown in Fig. 8. To make easier comparisons between different cases, we also plot results of the neutral case (Ha = 0), Fig. 8(a), as well as the case with electrically insulated walls ($C_d = 0$), Fig. 8(b) that are already discussed above. It is striking that even a relatively small wall conductance parameter ($C_d = 0.05$) leads to a significant flow reorganization, as shown in Fig. 8(c). The upper and lower rolls are significantly reduced in the vertical

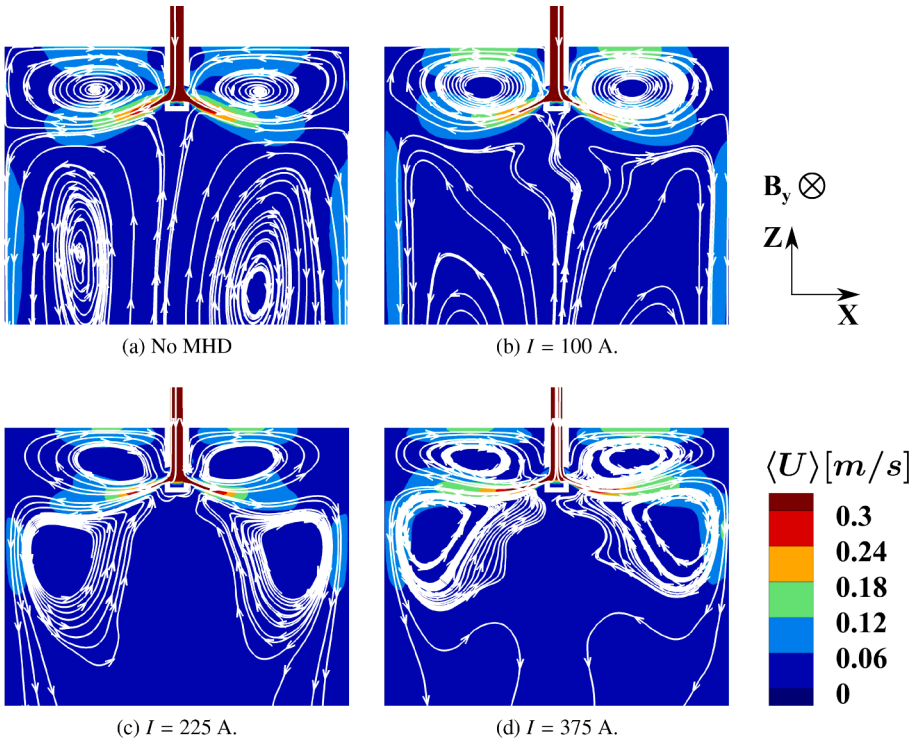

Fig. 5. The contours of time-averaged velocity magnitude superimposed with the velocity streamlines (white lines) in the central vertical ($y = 0$ m) cross-section (upper half of the mold) for the range of EMBr strength and fixed $C_d = 0$ (electrically insulated walls).

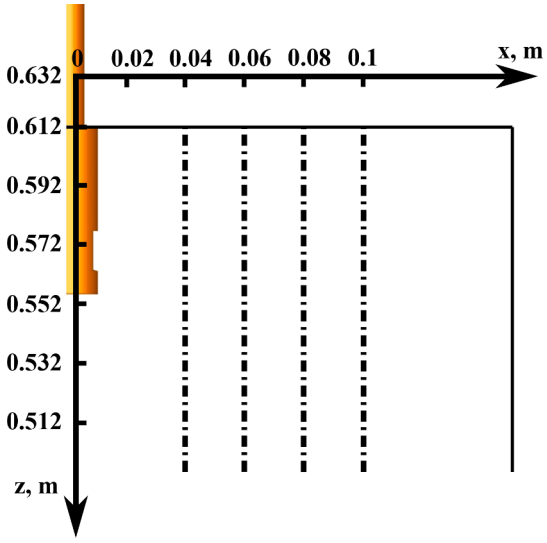

Fig. 6. A sketch of the locations in the central-vertical plane ($y = 0$ m) for which characteristic velocity profiles are extracted along the following co-ordinates: $x = 0.04$, 0.06, 0.08 and 0.1 m.

direction. The centers of the upper rolls are shifted away from the SEN, while the situation is opposite for the lower rolls. The penetrative depth of the incoming angular jet also increased. With further increase of the $C_d = 0.15$, much weaker upper and lower rolls are generated, Fig. 8(d). At the same time, the penetrative depth of the angular incoming jets also weakens. This reduction of the penetrative depth is even more clear for $C_d = 0.5$ case, while the incoming jet angle stays unchanged. Finally, for the fully conducting Hartmann walls, the upper rolls can not be observed anymore, and the penetrative depth of the incoming jet is reduced further, Fig. 8(e).

To provide a more detailed way of comparing the observed changes of the flow, we extract the maximum of the mean velocity magnitude in the central vertical plane ($y = 0$ m) along the selected vertical profiles at fixed values of x = 0.04, 0.06, 0.08 and 0.1 m, respectively, as illustrated in Fig. 9. We focus on the effects of the wall conducting ratio (C_d) for a fixed value of applied current $I = 225$ A) and show obtained results in Fig. 9. For all four locations, we observe a distinct non-linear behavior. For the first location (x = 0.04 m), the initial value of the neutral case initially increases until reaching a peak value (at $C_d = 0.1$), followed initially by a gradual decrease before reaching a final value (note that there is a slight increase as $C_d \to \infty$). The remaining three locations (x = 0.06, 0.08, and 0.1 m) - all show qualitatively similar behavior, starting with an initial suppression of the maximum of the velocity magnitude immediately upon activation of the magnetic field for the electrically insulated case ($C_d = 0$). All distributions are reaching the local peak in the $0.01 \leqslant C_d \leqslant 0.1$ interval, followed by initially very rapid decay (up to $C_d = 1$). After that value, a gradual mild increase is observed with a further increase of C_d. The slopes of the $\langle U_{max} \rangle$ versus C_d curves are showing the largest gradients at distances farther away from the SEN, i. e. at $x = 0.08$ and 0.1 m The observed non-monotonic behavior of the local maxima of the velocity magnitude can be explained in terms of the double rolls reorganization. and the corresponding stretching of the incoming jets. Also, this behavior should be included in the analysis of optimization of the incoming jet spreading, since too strong jets can distort the solidifying regions along the vertical walls. To achieve a stable double roll flow structure and significantly reduced penetrative strength of the incoming jets, one has to keep the wall conductance ratio parameter close to unity.

Another important flow region for the continuous casting is the meniscus zone. Here, strong upper rolls can break the upper slag layer at the top surface and cause unwanted entrainment of impurities towards the rest of the mold. Because of its importance, we analyze next the effects of the wall conductivities on the flow at the meniscus, Fig. 10. Here, we plot the contours of the horizontal mean velocity $\langle U_x \rangle$ to capture potential changes in the flow direction caused by the various wall conductivities. For the non-MHD case, the flow at the meniscus is

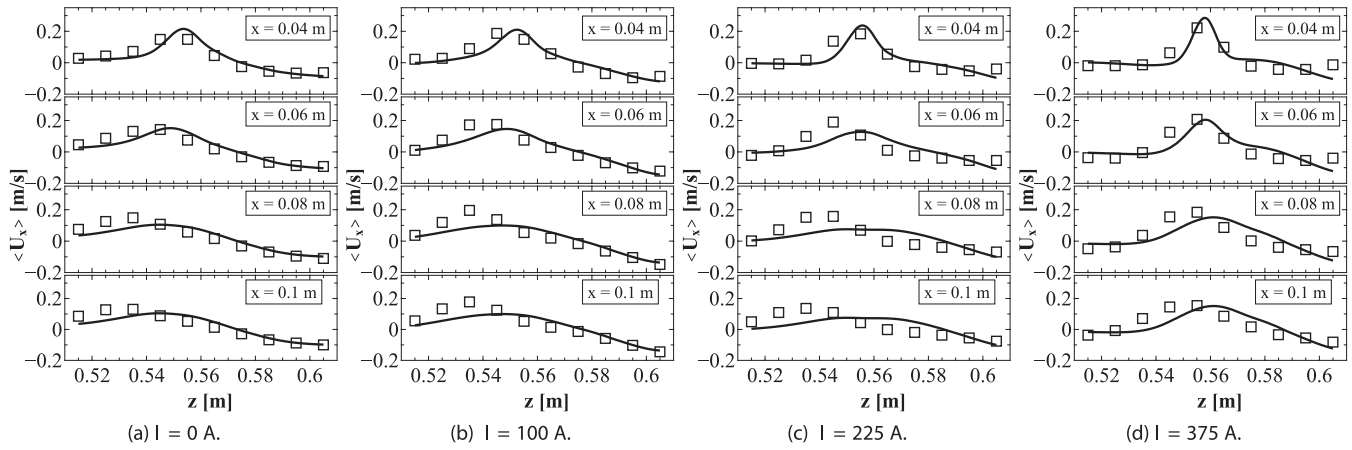

Fig. 7. The profiles of the time- and spatially-averaged horizontal (x-direction) velocity component at characteristic locations indicated in Fig. 6 in the range $0 \leqslant I \leqslant$ 375 A and fixed $C_d = 0$. The following indication is used: (——) – the present numerical study, (□) – the experimental results.

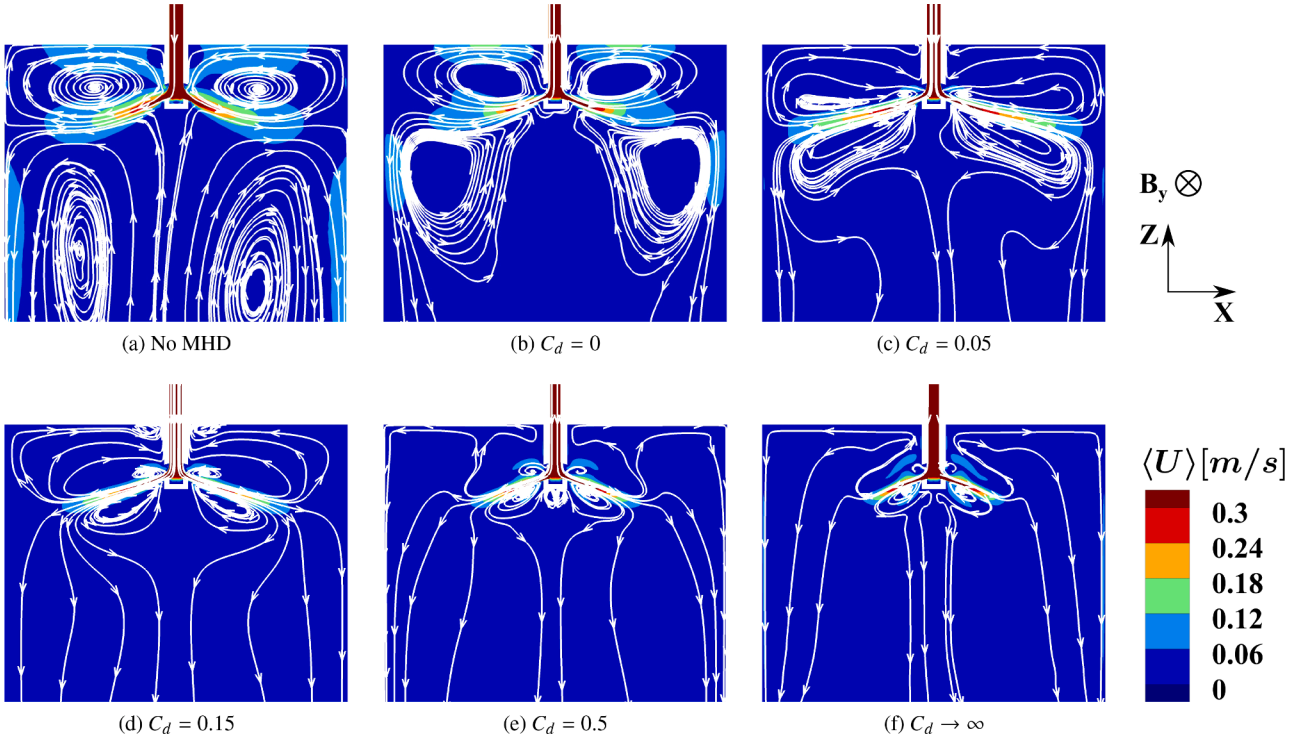

Fig. 8. The superimposed contours of the long-term time-averaged velocity magnitude and streamlines (white lines) in the central vertical ($y = 0$ m) cross-section (upper half of the mold) for the range of C_d parameter and the specific EMBr strength of $I = 225$ A.

directed towards the SEN, Fig. 10(a). By activating the magnetic field and increasing the wall conductivity the horizontal velocity gradually weakens (Figs. 10(b)-(d)), till a critical value of $C_d = 0.5$ is achieved, causing the flow reversal, Fig. 10(e). Further increase in C_d produces even stronger reversed flow at the meniscus, Fig. 10(f). To provide a more quantitative insight into the strength of the flow at the top surface, we extract the maximum values of the horizontal velocity for various wall conductivities, as shown in Fig. 11. It can be seen that very similar values are obtained for the non-MHD and MHD with $C_d = 0$. Further increase of the C_d results in a rapid suppression, with an almost non-moving top surface for the $C_d \approx 0.5$. It can be concluded that the most efficient suppression of the horizontal velocity at the meniscus is obtained in the $0.2 \leqslant C_d \leqslant 1$ range, which is useful information for a future design on the continuous casting set-ups. One should note the main difference in the MHD interaction mechanism between simulations from above-mentioned groups I and II. For the cases belonging to group I, the resulting Lorentz force distribution is directly affected by strength of the imposed EMBr (i.e. strength of the magnetic field). In contrast to this, for the cases belonging to group II, the resulting Lorentz force is additionally affected by rearrangement of the current density streamlines caused by the finite electric conductivity of the walls. Now, instead of having fully closed loops of the electric current density streamlines within the fluid domain (for the electrically insulated walls), the electric current also penetrates solid walls, as shown in Fig. 12. With higher wall conductivity, the more current density enters the solid region, and current streamlines now loop over both flow and wall domains. This reorganization of the electric current density changes the local Lorentz force distribution, and finally, the velocity field. To provide additional insights into underlying MHD variables, contours of the mean electric potential in the central vertical plane are shown in Fig. 13. Starting from

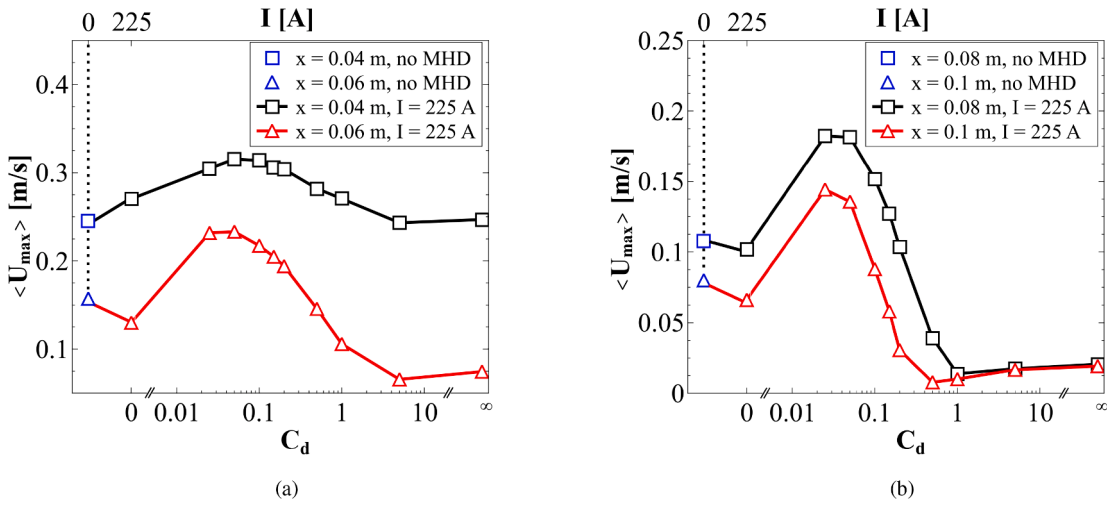

Fig. 9. Dependency of the maximum magnitude of the mean velocity in the vertical ($y = 0$ m) cross-section with the horizontal coordinates of (a) $x = 0.04$ m and $x = 0.06$ m and (b) $x = 0.08$ m and $x = 0.1$ m on the wall conductivity ratio parameter C_d at the specific EMBr strength of $I = 225$ A. The relative position of the cross-sections is indicated in Fig. 6.

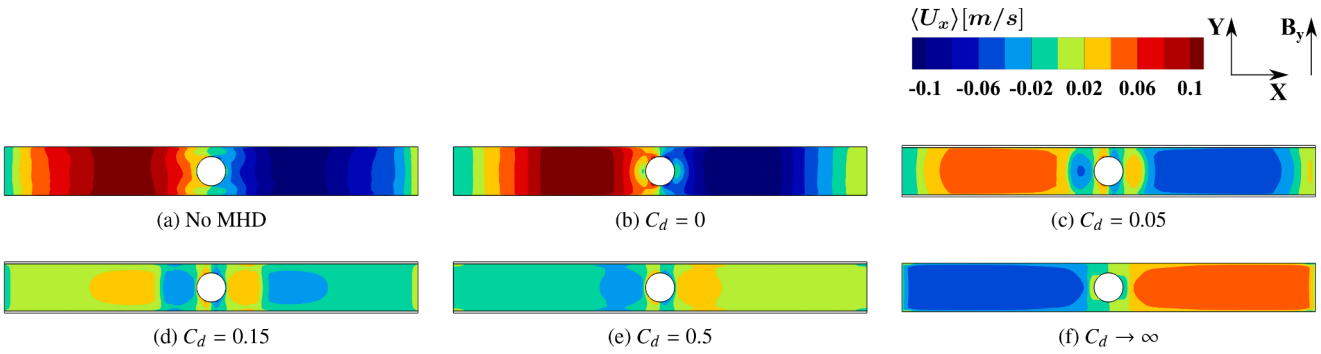

Fig. 10. The contours of the time-averaged horizontal velocity at the meniscus for the range of C_d parameters and the specific EMBr strength of $I = 225$ A.

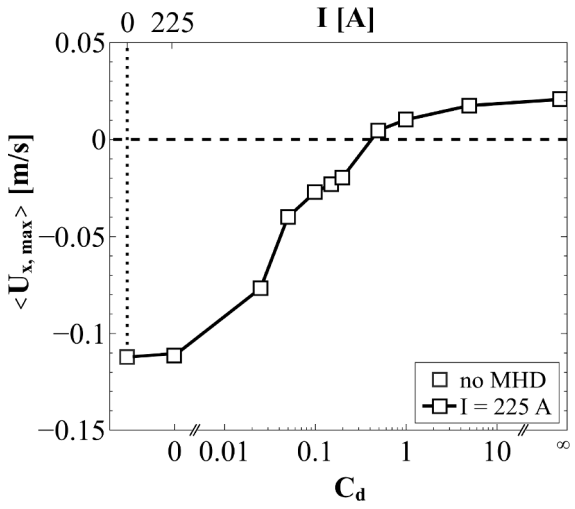

Fig. 11. Dependency of the meniscus maximum mean horizontal (x) velocity on the wall conductivity ratio C_d, at the specific EMBr strength of $I = 225$ A. The relative position of the cross-sections is indicated in Fig. 6.

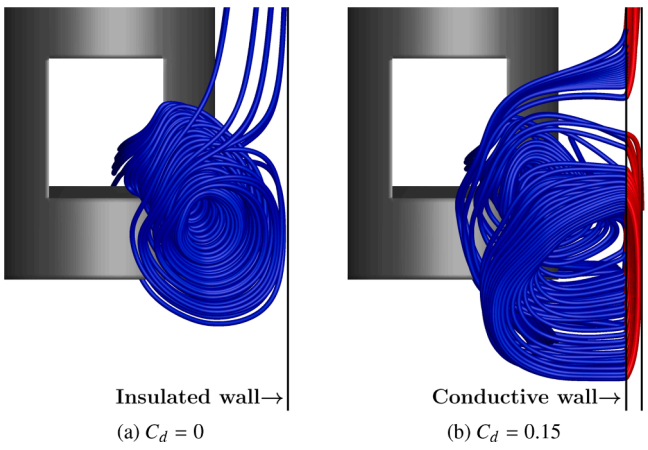

Fig. 12. Visualization of the three-dimensional time-averaged electric current density streamlines in the vicinity of the bottom right corner of the SEN port for the electrically insulated ($C_d = 0$) (a) and Hartmann walls with finite conductivity ($C_d = 0.15$) (b). Note that color indicates distribution within the flow region (blue) or solid wall (red).

the fully electrically insulated case ($C_d = 0$), it can be seen that local maxima and minima coincide with the locations of the flow loops, Fig. 13(b). By increasing C_d, these distinct regions get reduced in size, Fig. 8(c)-(f). This behavior is expected since the source of electric potential is the cross product of the magnetic field and local velocity, and distributions of electrical potential closely follow the above-analyzed velocity fields shown in Fig. 8.

Previous studies indicate that the flow in the mold can be influenced

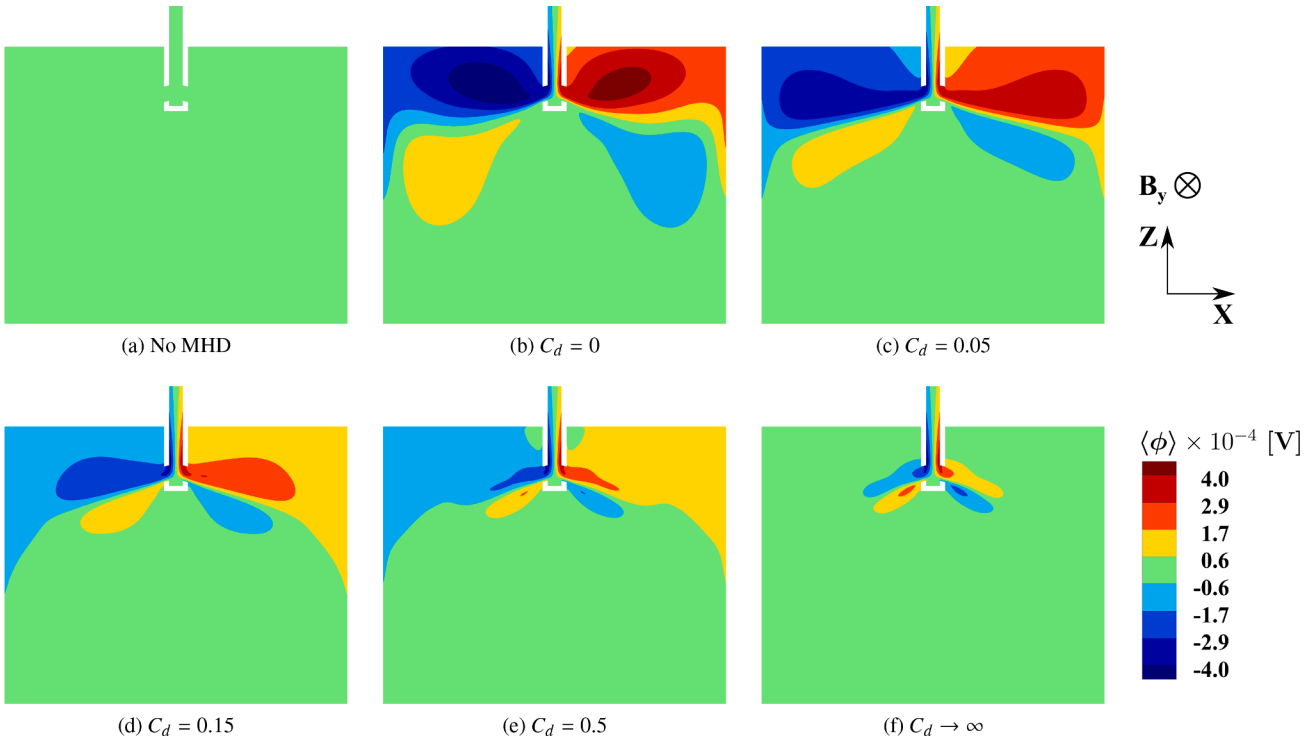

Fig. 13. The contours of the time-averaged electric potential in the central vertical ($y = 0$ m) cross-section (upper half of the mold) for the range of C_d parameters and fixed EMBr strength of $I = 225$ A.

by several control mechanisms, such as argon bubbles injections (Santos et al., 2020), different strength of the magnetic field (Vakhrushev et al., 2021; Schurmann et al., 2018; Kubota et al., 2001), and the position of the stopper-rod (Chaudhary et al., 2011). The mechanism presented in this work, which consists in using various C_d, differs qualitatively from the mechanisms previously reported in the literature and can be potentially used to obtain a necessary flow structure.

4.3. The influence of the wall conductivity on the turbulence and instantaneous coherent structures

Next, we move to analyze in detail the effects of the wall conductance also on the resolved turbulence. The contours of the long-term time-averaged resolved turbulent kinetic energy (TKE) are shown in Fig. 14. It can be seen that the predominantly turbulent regions are generated in

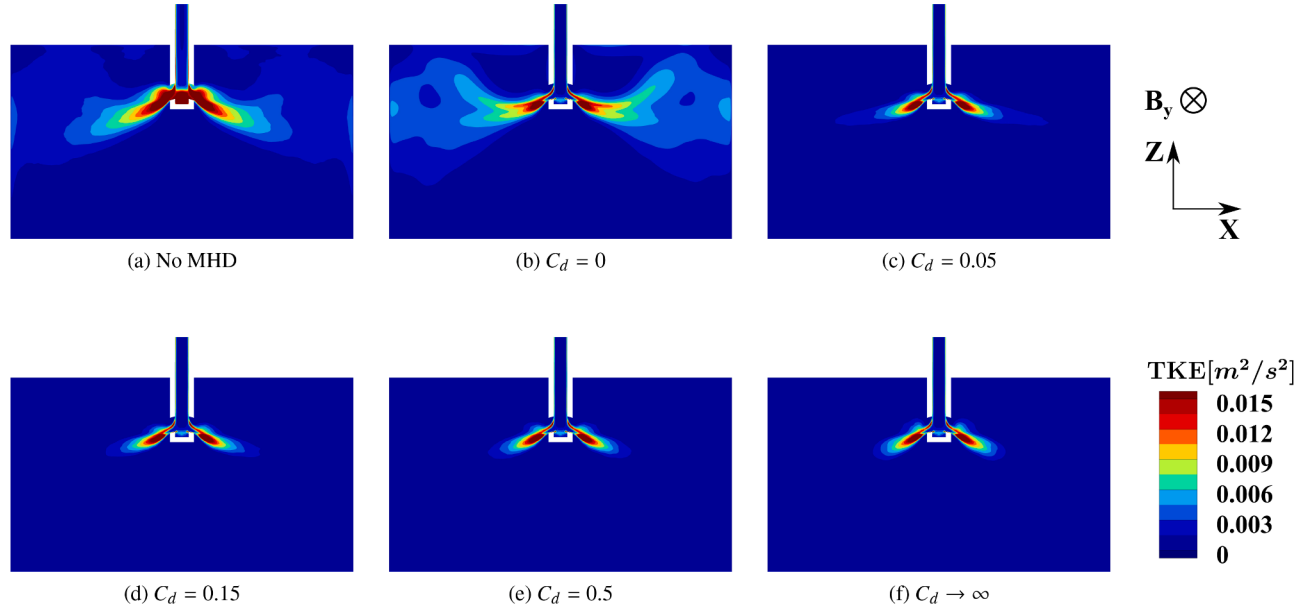

Fig. 14. The contours of the long-term time-averaged resolved turbulent kinetic energy (TKE) in the central vertical ($y = 0$ m) cross-section (upper half of the mold) for the range of C_d parameters and fixed EMBr strength of $I = 225$ A.

the bifurcating jet regions for all considered wall conductivities. In addition, for the non-MHD case, the TKE is also high inside the port where the remaining incoming flow after bifurcations impinges on the bottom part. Compared to the neutral no-MHD case, Fig. 14(a), activation of the magnetic field causes an extension of the turbulence dominated regions towards the sidewalls and in the proximity of the top surface, while the strong suppression is observed inside the SEN, Fig. 14 (b). Activation of the finite wall conductance, even with a relatively low value of $C_d = 0.05$, significantly alters this initial distribution and a significant reduction of turbulent regions can be observed, Fig. 14(c). Further increase of the wall conductance (i.e. $0.15 \leqslant C_d \rightarrow \infty$) produces just marginal effects on the TKE distribution, indicating that a saturation point of turbulence reorganization and suppression is achieved, as seen in Figs. 14(d-f).

We close our analysis by finally providing some detailed insights into instantaneous flow and turbulence behavior for different wall conductivities. To represent qualitatively the instantaneous three-dimensional flow structures, we adopt the Q-criterion (i.e. the second-invariant of the velocity gradient tensor), as shown in Fig. 15. The non-MHD case exhibits the most dense patterns, indicating a strong interaction between the bifurcating jets and the free surface regions, Fig. 15(a). Activation of the EMBr with $C_d = 0$ generates less populated coherent structure regions with distinct asymmetrical distribution of the bifurcating jets, Fig. 15(b). Note that size of coherent structures in the bifurcating jets increases in comparison with the neutral case. In contrast to the fully electrically insulated walls ($C_d = 0$) case, the embedding of electrically conducting walls with $C_d = 0.05$ almost eliminates the long cylindrical-shaped vortices, while remaining coherent structures are mainly concentrated in the bifurcating jets, Fig. 15(c). With further increase of C_d, the coherent structures are suppressed and clustered in the horizontally reduced bifurcating jet regions, Fig. 15(d-f).

To provide information on the temporal behavior of the bifurcating jets for different values of the wall conductivities, we analyze the time-series of the velocity magnitude at a particular monitoring point (similar to Kenjereš et al., 2011; Kenjereš, 2012): (i) the 'jet' probe located in the jet proximity with the following coordinates $p_j(0.1, 0, 0.54)$ m, and (ii) the 'meniscus' probe located in the proximity of the top surface with the following coordinates $p_m(0.1, 0, 0.605)$ m, as indicated in Fig. 16. The selected monitoring locations are placed in flow regions that are the most sensitive to the flow oscillations.

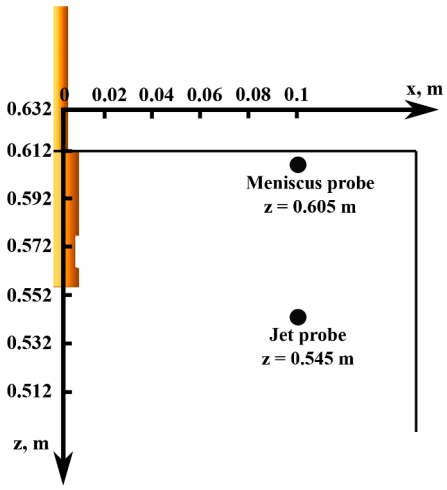

Fig. 16. The locations of selected monitoring points (probes) in the jet and close to meniscus regions - both in the central vertical ($y = 0$ m) cross-section.

The time evolutions (over a time interval of 70 s) of the velocity magnitude at characteristic monitoring points, for various values of C_d, are shown in Fig. 17. The presented signals illustrate the large-scale

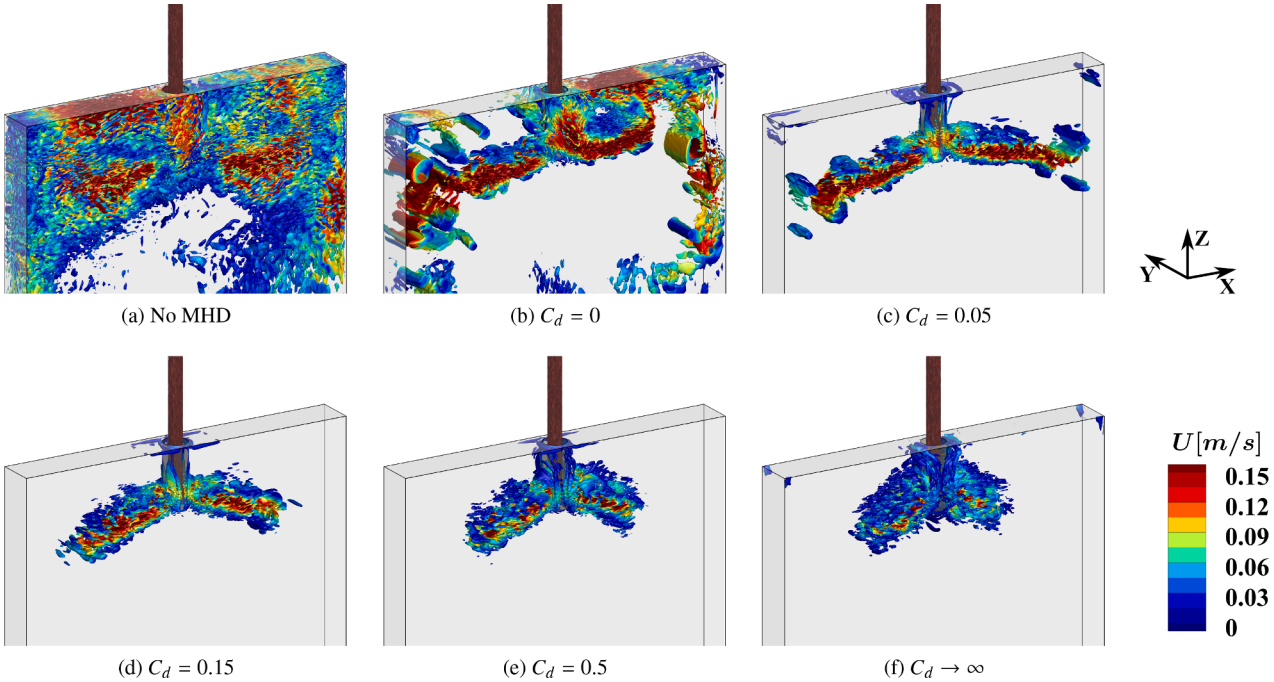

(a) No MHD (b) $C_d = 0$ (c) $C_d = 0.05$

(d) $C_d = 0.15$ (e) $C_d = 0.5$ (f) $C_d \rightarrow \infty$

Fig. 15. The isosurfaces of the second-invariant of the velocity gradient tensor (Q-criterion, Q $= 20\ s^{-2}$) colored by instantaneous velocity magnitude for the range of C_d parameters and fixed EMBr strength of $I = 225$ A.

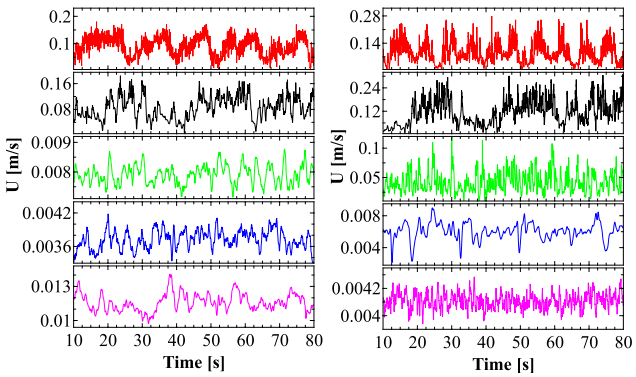

(a) The meniscus probe. (b) The jet probe.

Fig. 17. Time series of velocity magnitude for the various C_d parameters and fixed EMBr strength of $I = 225$ A in two monitoring points (as indicated in Fig. 16): (a) the meniscus prove; (b) the jet probe. The following lines are used: (—) – no MHD ($I = 0$ A) case; (—·) - $I = 225$ A, $C_d = 0$; (—) – $I = 225$ A, $C_d = 0.15$; (—) – $I = 225$ A, $C_d = 0.5$; (—) – $I = 225$ A, $C_d \to \infty$.

vertical (along the z-direction) oscillations of jets emanating from the SEN. It can be seen that both the magnitude and the frequency of presented signals are significantly modified by changing C_d. We calculate the power spectral density (PSD) of these signals by performing a discrete Fourier transformation, and results are shown in Fig. 18. Note that to get a better overview of distributions, each spectrum after the non-MHD case is shifted relative to the previous one with a factor of 1/10. For both the sub-meniscus and jet probes, we also indicate characteristic −5/3 Kolmogorov (black dashed lines) and −10/3 viscous dissipation (black dot lines) slopes. It can be seen that both slopes are followed at both monitoring locations for the neutral non-MHD case, Figs. 17(a) and (b). For the sub-meniscus probe, activation of the EMBr with $C_d = 0$ introduces a significant extension of −5/3 slope (inertial) region (i.e. it starts earlier at significantly lower frequencies, $f \approx 1$ Hz), while −10/3 viscous dissipation region is significantly reduced, Figs. 18 (a). With a further increase of C_d, the −10/3 slope can not be observed anymore while the −5/3 slope (inertial cascade range) still extends over a significant range of frequencies (i.e. $0.2 \leqslant f \leqslant 10$ Hz). The PSD at the jet probe location for the non-MHD case also exhibits both −5/3 and −10/3 slopes, Fig. 18(b). However, in contrast to the sub-meniscus probe, here the −10/3 slope still can be observed for up to $C_d = 0.5$. Both the inertial and dissipation range are shifted to the lower frequencies with an increase of the wall conductivity ratio, similarly to the sub-meniscus location.

To obtain and compare distinct frequencies of the flow, we extract this information from the above-presented PSD plots and collect them in Table 2. For the sub-meniscus probe, a dominant frequency of $f_1 = 0.07$

Table 2
List of dominant and secondary frequencies based on the power spectral density at the meniscus probe and the jet probe. The position of the probes is shown in Fig. 16.

C_d, Hartmann walls	Meniscus probe, frequency, Hz	Jet probe, frequency, Hz
no MHD	$f_1 = 0.07$	$f_1 = 0.15$
0	$f_1 = 0.042$	$f_1 = 0.035$
0.15	$f_1 = 0.21$ $f_2 = 0.12$ $f_3 = 0.25$	$f_1 = 0.17$ $f_2 = 0.61$ $f_3 = 1.2$
0.5	$f_1 = 0.12$ $f_2 = 0.087$ $f_3 = 0.18$	$f_1 = 0.21$ $f_2 = 0.16$ $f_3 = 0.11$
∞	$f_1 = 0.03$ $f_2 = 0.057$	$f_1 = 0.06$ $f_2 = 0.087$

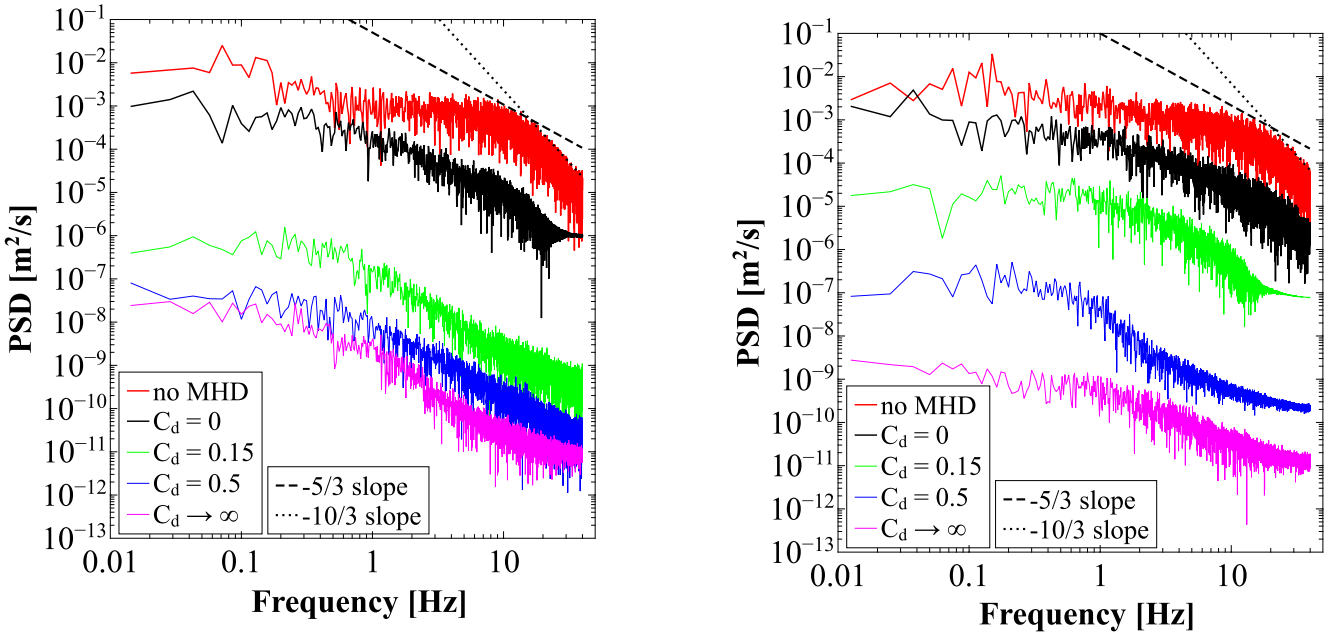

(a) (b)

Fig. 18. Dependency of the power spectral density (PSD) on the frequency at (a) the meniscus probe and (b) the jet probe (locations are shown in Fig. 16) for the range of C_d parameters and fixed EMBr strength o.f $I = 225$ A.

Hz is observed for the non-MHD case. With EMBr activation, this dominant frequency shifts to $f_1 = 0.042$ Hz. Theses relatively low frequencies indicate the presence of the extremely long-time preserving unsteady flow behavior, which implies that special care should be taken for a proper collection of the flow first- and second-moments. For $C_d = 0.15$, the most dominant frequency is significantly shifted to $f_1 = 0.21$ Hz, followed with appearance of secondary frequencies at $f_2 = 0.12$ Hz and $f_3 = 0.25$ Hz, respectively. Finally, for $C_d = 0.5$ and $C_d \to \infty$ cases, the dominant frequencies are shifted back to $f_1 = 0.12$ Hz and $f_1 = 0.03$ Hz, respectively. For the jet probe, the imposing the EMBr with $C_d = 0$ again produces a reduction of the dominant frequency compared to the neutral non-MHD case, i.e. from $f_1 = 0.15$ Hz to $f_1 = 0.035$ Hz. With further increase of $C_d = 0.15$ and $C_d = 0.5$, multiple secondary frequencies (f_2 and f_3) are also observed. Finally, for $C_d \to \infty$, the most dominant frequency is shifted back to $f_1 = 0.06$ Hz. To conclude, the jet probe indicates the existence of the long-term low-frequency flow oscillations for the non-MHD and fully electrically insulated MHD case ($C_d = 0$). Activation of the finite wall conductance removes these long-term fluctuations ($C_d = 0.15$ and 0.5). However, application of the perfectly conducting walls ($C_d \to \infty$) promotes again a return of long-term low-frequency flow oscillations.

5. Summary and conclusion

We have presented a comprehensive numerical study on effects of the electric wall conductivity on behavior of a turbulent electrically conducting liquid alloy flow subjected to an external magnetic field - mimicking experimental setup of the Mini-LIMMCAST casting mold. We have applied an advanced in–house developed conjugate MHD extended Navier–Stokes solver based on open-source OpenFOAM code. The solver is based on the inductionless assumption of the generated magnetic field (i.e. one-way coupling between the momentum and imposed magnetic field) in a combination with the Large-Eddy Simulation approach employing the dynamic subgrid closure for unresolved turbulent stresses. We have performed a series of numerical simulations that include the neutral (non-MHD) and MHD cases with various imposed EMBr (latter with the fully electrically insulating walls) and compared obtained results with the experimental data. A good agreement between simulations and experiments of the characteristic horizontal component of the mean velocity profiles at different locations is obtained for both non-MHD and MHD cases for various strengths of the imposed EMBr for fully electrically insulated walls. Next, we considered an extensive range of the wall conductivity ratio parameter ($0.025 \leqslant C_d < \infty$) and analyzed its effects on the flow and turbulence inside the mold. We have shown that with increasing the wall conductivity ratio of the Hartmann walls a significant reorganization of the initial double-roll flow structure takes place. This flow reorganization was also followed by significant suppression of the flow oscillations. We have observed a non-monotonic behavior of the mean velocity magnitude maximum at all selected profiles in the central vertical plane. This non-monotonic behavior also indicated generation of the enhanced side-jets in the $0.025 \leqslant C_d < 1$ range, while the strongest mean velocity suppression was obtained for $C_d \approx 1$. In addition, we have demonstrated that the velocity in the proximity of the top-surface (i.e. the sub-meniscus region) showed high sensitivity to the presence of the electrically conducting walls. The maximum velocity was obtained in the $0.2 \leqslant C_d \leqslant 1$ range, whereas the flow reversal was taking place with a further increase of C_d. The power spectral density analysis of the instantaneous velocity magnitude at two characteristic monitoring locations, placed in the side-jet and the vicinity of the meniscus revealed the existence of flow oscillations with a very low frequency for the neutral (non-MHD) and MHD case with perfectly electrically insulated walls ($C_d = 0$). This low frequency was not observed for the MHD cases with $0.15 \leqslant C_d \leqslant 0.5$. However, for the perfectly electrically conducting walls case ($C_d \to \infty$), the long-term low-frequency flow oscillation reappeared.

Practical implementation of various C_d can be possible by changing the mold parameters such as the mold width, though high values of the wall conductivity ratio ($C_d > 1$) will be challenging to achieve. The alternative way will be changing the size of the EMBr. The presented results can provide important designing guidelines for the new generation of the laboratory- and real-scale industrial continuous casting setups.

CRediT authorship contribution statement

Artem Blishchik: Conceptualization, Methodology, Software, Validation, Formal analysis, Investigation, Data curation, Visualization, Writing - original draft. **Ivan Glavinić:** Conceptualization, Data curation, Investigation, Validation, Resources, Writing - original draft. **Thomas Wondrak:** Conceptualization, Data curation, Investigation, Validation, Resources, Writing - review & editing, Supervision. **Daniel van Odyck:** Conceptualization, Methodology, Software, Validation, Investigation, Data curation, Writing - review & editing, Supervision. **Saša Kenjereš:** Conceptualization, Investigation, Visualization, Resources, Writing - review & editing, Supervision, Funding acquisition, Project administration.

Declaration of Competing Interest

The authors declare that they have no known competing financial interests or personal relationships that could have appeared to influence the work reported in this paper.

Acknowledgments

This project has received funding from the European Union's Horizon 2020 research and innovation program TOMOCON (Smart Tomographic Sensors for Advanced Industrial Process Control) under the Marie Sklodowska-Curie grant agreement No.764902.

Appendix A. Appendix

The investigation of the mesh influence on the obtained solution is shown in Fig. A.19, for the case with the EMBr strength of $I = 375$ A. Three already mentioned grids have been tested: the coarse mesh $M_{L,coarse}$, the intermediate mesh M_L, and the fine mesh $M_{L,fine}$. As it can be seen, the difference between the M_L and $M_{L,fine}$ is marginal, and therefore the results obtained with the intermediate mesh can be declared as the grid-independent.

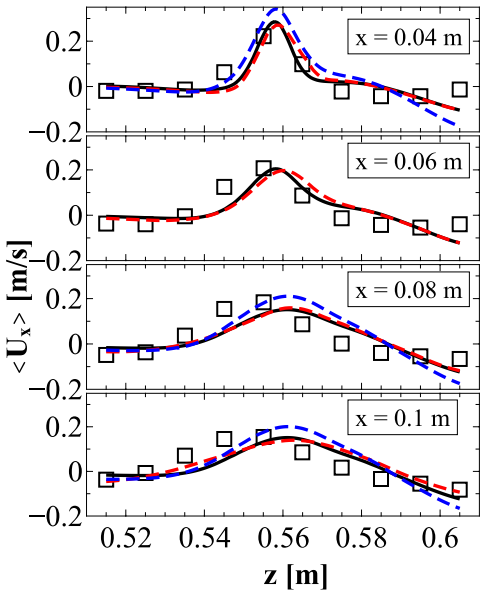

Fig. A.19. The profiles of the long-term time- and spatially-averaged horizontal velocity obtained at various grids at $I = 375$ A and $C_d = 0$. The following notation is used: (□) – the experimental results; (– –) – the coarse mesh $M_{L,coarse}$; (—) – the main intermediate mesh; M_L (– –) – the fine mesh. $M_{L,fine}$.

References

Abouelazayem, S., Glavinic, I., Wondrak, T., Hlava, J., 2020. Flow control based on feature extraction in continuous casting process. Sensors 20 (23).

Blishchik, A., van der Lans, M., Kenjereš, S., 2021. An extensive numerical benchmark of the various magnetohydrodynamic flows. Int. J. Heat Fluid Flow 90, 108800.

Blishchik, A., Kenjereš, S., 2021. Observation of a novel flow regime caused by finite electric wall conductance in an initially turbulent magnetohydrodynamic duct flow. Phys. Rev. E 104 (1). L013101:1-6.

Chaudhary, R., Lee, G.-G., Thomas, B.G., Cho, S.-M., Kim, S.-H., Kwon, O.-D., 2011. Effect of stopper-rod misalignment on fluid flow in continuous casting of steel. Metall. Mater. Trans. B 42 (2), 300–315.

Chaudhary, R., Thomas, B.G., Vanka, S.P., 2012. Effect of electromagnetic ruler braking (embr) on transient turbulent flow in continuous slab casting using large eddy simulations. Metall. Mater. Trans. B 9, 532–553.

Davidson, P.A., 2001. An Introduction to Magnetohydrodynamics, Cambridge Texts in Applied Mathematics. Cambridge University Press.

Graebe, S., Goodwin, G., Elsley, G., 1995. Control design and implementation in continuous steel casting. IEEE Control Syst. Mag. 15 (4), 64–71.

Issa, R., Gosman, A., Watkins, A., 1986. The computation of compressible and incompressible recirculating flows by a non-iterative implicit scheme. J. Comput. Phys. 62 (1), 66–82.

Kenjereš, S., 2012. Energy spectra and turbulence generation in the wake of magnetic obstacles. Phys. Fluids 24 (11), 115111:1-19.

Kenjereš, S., 2018. On modeling and eddy-resolving simulations of flow, turbulence, mixing and heat transfer of electrically conducting and magnetizing fluids: A review. Int. J. Heat Fluid Flow 73, 270–297.

Kenjereš, S., ten Cate, S., Voesenek, C.J., 2011. Vortical structures and turbulent bursts behind magnetic obstacles in transitional flow regimes. Int. J. Heat Fluid Flow 32 (3), 510–528.

Krasnov, D., Zikanov, O., Schumacher, J., Boeck, T., 2008. Magnetohydrodynamic turbulence in a channel with spanwise magnetic field. Phys. Fluids 20 (9), 095105.

Kubota, J., Kubo, N., Ishii, T., Suzuki, M., Aramaki, N., Nishimachi, R., 2001. Steel flow control in continuous slab caster mold by traveling magnetic field. NKK Tech. Rev. (Japan) 85, 1–9.

Lilly, D.K., 1992. A proposed modification of the Germano subgrid-scale closure method. Phys. Fluids A 4 (3), 633–635.

Li, F., Wang, E., Feng, M., Li, Z., 2015. Simulation research of flow field in continuous casting mold with vertical electromagnetic brake. ISIJ Int. 55 (4), 814–820.

Liu, Z., Vakhrushev, A., Wu, M., Karimi-Sibaki, E., Kharicha, A., Ludwig, A., Li, B., 2018. Effect of an electrically-conducting wall on transient magnetohydrodynamic flow in a continuous-casting mold with an electromagnetic brake. Metals 8 (8).

Miao, X., Timmel, K., Lucas, D., Ren, Z., Eckert, S., Gerbeth, G., 2012. Effect of an electromagnetic brake on the turbulent melt flow in a continuous-casting mold. Metall. Mater. Trans. B 43, 954–972.

Mistrangelo, C., Bühler, L., 2011. Development of a numerical tool to simulate magnetohydrodynamic interactions of liquid metals with strong applied magnetic fields. Fusion Sci. Technol. 60 (2), 798–803.

Muttakin, I., Soleimani, M., 2020. Magnetic induction tomography spectroscopy for structural and functional characterization in metallic materials. Materials 13 (11).

Ni, M.-J., Munipalli, R., Huang, P., Morley, N.B., Abdou, M.A., 2007. A current density conservative scheme for incompressible mhd flows at a low magnetic Reynolds number. Part II: On an arbitrary collocated mesh. J. Comput. Phys. 227 (1), 205–228.

Plevachuk, Y., Sklyarchuk, V., Eckert, S., Gerbeth, G., Novakovic, R., 2014. Thermophysical properties of the liquid ga-in-sn eutectic alloy. J. Chem. Eng. Data 59 (3), 757–763.

Righolt, B.W., Kenjereš, S., Kalter, R., Tummers, M.J., Kleijn, C.R., 2015. Dynamics of an oscillating turbulent jet in a confined cavity. Phys. Fluids 27 (9), 095107.

Santos Jr, P.L., Peixoto, J.J.M., da Silva, C.A., da Silva, I.A., Galinari, C.M., 2020. Bubble behavior in the slab continuous casting mold: Physical and mathematical model. J. Mater. Res. Technol. 9 (3), 4717–4726.

Sarkar, S., Singh, V., Ajmani, S.K., Singh, R.K., Chacko, E.Z., 2018. Effect of argon injection in meniscus flow and turbulence intensity distribution in continuous slab casting mold under the influence of double ruler magnetic field. ISIJ Int. 58 (1), 68–77.

Schurmann, D., Glavinic, I., Willers, B., Timmel, K., Eckert, S., 2018. Impact of the electromagnetic brake position on the flow structure in a slab continuous casting mold: An experimental parameter study. Metall. Mater. Trans. B.

Schurmann, D., Willers, B., Hackl, G., Tang, Y., Eckert, S., 2019. Experimental study of the mold flow induced by a swirling flow nozzle and electromagnetic stirring for continuous casting of round blooms. Metall. Mater. Trans. B 50, 716–731.

Spalding, D., 1961. A single formula for the law of the wall. J. Appl. Mech. 28, 455–458.

Smolentsev, S., Moreau, R., Bühler, L., Mistrangelo, C., 2010. Mhd thermofluid issues of liquid-metal blankets: Phenomena and advances. Fusion Eng. Des. 85 (7), 1196–1205.

Thomas, B.G., Chaudhary, R., 2009. State of the art in electromagnetic flow control in continuous casting of steel slabs: Modeling and plant validation, 6th International Conference on Electromagnetic Processing of Materials EPM.

Thomas, B.G., Zhang, L., 2001. Mathematical modeling of fluid flow in continuous casting. ISIJ Int. 41 (10), 1181–1193.

Timmel, K., Eckert, S., Gerbeth, G., 2010. Experimental investigation of the flow in a continuous-casting mold under the influence of a transverse, direct current magnetic field. Metall. Mater. Trans. B 42 (1), 68–80.

Vakhrushev, A., Kharicha, A., Liu, Z., Wu, M., Ludwig, A., Nitzl, G., Tang, Y., Hackl, G., Watzinger, J., 2020. Electric current distribution during electromagnetic braking in continuous casting. Metall. Mater. Trans. B 51 (6), 2811–2828.

Vakhrushev, A., Kharicha, A., Karimi-Sibaki, E., Wu, M., Ludwig, A., Nitzl, G., Tang, Y., Hackl, G., Watzinger, J., Eckert, S., 2021. Generation of reverse meniscus flow by applying an electromagnetic brake. Metall. Mater. Trans. B 52 (5), 3193–3207.

Weber, N., Beckstein, P., Galindo, V., Starace, M., Weier, T., 2018. Electro-vortex flow simulation using coupled meshes. Comput. Fluids 168, 101–109.

Weller, H.G., Tabor, G., Jasak, H., Fureby, C., 1998. A tensorial approach to computational continuum mechanics using object-oriented techniques. Comput. Phys. 12 (6), 620–631.
Wondrak, T., Eckert, S., Gerbeth, G., Klotsche, K., Stefani, F., Timmel, K., Peyton, A.J., Terzija, N., Yin, W., 2011. Combined electromagnetic tomography for determining two-phase flow characteristics in the submerged entry nozzle and in the mold of a continuous casting model. Metall. Mater. Trans. B 42 (6), 1201–1210.
Zhang, L., Aoki, J., Thomas, B.G., 2006. Inclusion removal by bubble flotation in a continuous casting mold. Metall. Mater. Trans. B 37, 361–379.
Zhang, K., Weeks, M., Roberts, P., 2004. Effect of electrically conducting walls on rotating magnetoconvection. Phys. Fluids 16 (6), 2023–2032.